# Fast Measurement of Surface Topographies Using a Phase-Measuring Deflectometric Microscopy

Zhifei Hu, Xiangchao Zhang, *Member, IEEE*, Wei Lang, Yunuo Chen, Ting Chen, and Min Xu

***Abstract*—With the fast development in the fields of photovoltaics and integrated circuits, the measurement of surface topographies and micro-scaled defects has attracted intensive interests. However, existing measurement methods are time-consuming and unsuitable for in-situ detection. Therefore, a fast topographic measurement method is developed based on the deflectometric microscope system. Microscopic deflectometry is an attractive tool due to its high sensibility to surface slopes and large dynamic range of measurement. For the quantitative reconstruction of surface topographies from slopes, an integration method is developed based on the minimum spanning tree, and the integration path is designed based on a sparse representation and a curl map. The robustness and accuracy of the integration method are validated by numerical simulation and experiments. This method can achieve a high measurement accuracy with a high lateral resolution and a depth of field of 90 $\mu$m, hereby improving the manufacturing efficiency and quality of opto-electronics functional devices.**

***Index Terms*—Defect, deflectometry, in-situ measurement, surface reconstruction.**

## I. Introduction

THE quality control of opto-electronics functional surfaces is becoming increasingly important. During fabrication and utilization, the surface is prone to defects such as pits and scratches, which not only reduce the surface quality but also directly affect the performance of the entire system.

At present, plenty of qualitative defect detection methods have been developed, among which the human visual inspection method [1] is widely applied. However, this method has low efficiency and accuracy because it depends greatly on the operator's experience [2]. To solve these problems, the machine vision technique is developed using different image processing algorithms. Hara et al. [3] proposed to identify the local features on the tested samples by comparing with reference patterns. Unfortunately, these methods may have unsatisfactory performance for complex features of defects, because they are manually and specifically designed, but not universally applicable. Some researchers realized automated feature detection from raw data by deep learning. Liu et al. [4] established Deep Belief Networks (DBN) for high-accuracy defect detection. But collecting training datasets is costly. Ren et al. [5] developed a deep learning approach that requires a small training set. However, local features are ignored in this method, which leads to a poor performance in detecting shallow and low-contrast defects.

Instead of by direct optical imaging, some other optical characteristics can also be utilized for defect detection, e.g., the polarization properties and refractive indices [6] and the single-sided diffraction of optical components [7]. However, none of these methods can solely provide reliable detection results. The dark-field imaging method is commonly applied [8], [9]. But it suffers from difficulties in identifying shallow scratches and small defects. Li et al. [10] developed a laser structured-light system. But this method is unable to detect micro-defects due to its limited resolution. Huang et al. [11] proposed a structured-light modulation analysis technique, which can detect defects on specular surfaces and transparent objects. In general, existing methods are mainly focused on the qualitative inspection such as classification, localization, and segmentation, which could not meet the needs of fast-developing opto-electronics industry. As a result, the quantitative measurement of micro-scaled topography is urgently demanded.

Currently, there are two kinds of techniques for the quantitative measurement of surface topography, namely the contact way and the non-contact way. Typical contact measurement instruments include Electrostatic Force Microscope, Atomic Force Microscope, and Magnetic Force Microscope [12], [13], [14]. They mainly contact the sample under test by using the probe as a sensor. These methods have the advantages of a high vertical resolution and a large dynamic range. However, they are very expensive and difficult to be utilized. Furthermore, it is laborious for finding the defects, and destructive to soft and fragile surfaces. Non-contact optical methods are applied in various fields because of their advantages of non-destructivity and rich information, such as confocal microscope and white light interferometry. However, these methods also have the disadvantages of high cost and low efficiency. Moreover, all these microscopic methods suffer from the depth of field (DOF) limitation, which in turn puts high requirements on precise

Manuscript received 18 December 2022; revised 24 January 2023; accepted 6 February 2023. Date of publication 15 February 2023; date of current version 27 February 2023. This work was supported in part by the National Natural Science Foundation of China under Grant 51875107 and in part by the Key Research and Development Program of Jiangsu Province under Grant BE2021035. *(Corresponding author: Xiangchao Zhang.)*

Zhifei Hu, Yunuo Chen, Ting Chen, and Min Xu are with the Shanghai Engineering Research Center of Ultra-Precision Optical Manufacturing, School of Information Science and Technology, Fudan University, Shanghai 200438, China (e-mail: 20210720016@fudan.edu.cn; 22110720005@m.fudan.edu.cn; 20110860002@fudan.edu.cn; minx@fudan.edu.cn).

Xiangchao Zhang and Wei Lang are with the Shanghai Engineering Research Center of Ultra-Precision Optical Manufacturing, School of Information Science and Technology, Fudan University, Shanghai 200438, China, and also with the Yiwu Research Institute, Fudan University, Zhejiang 322000, China (e-mail: zxchao@fudan.edu.cn; 21110720011@m.fudan.edu.cn).

Digital Object Identifier 10.1109/JPHOT.2023.3243736

This work is licensed under a Creative Commons Attribution 4.0 License. For more information, see https://creativecommons.org/licenses/by/4.0/

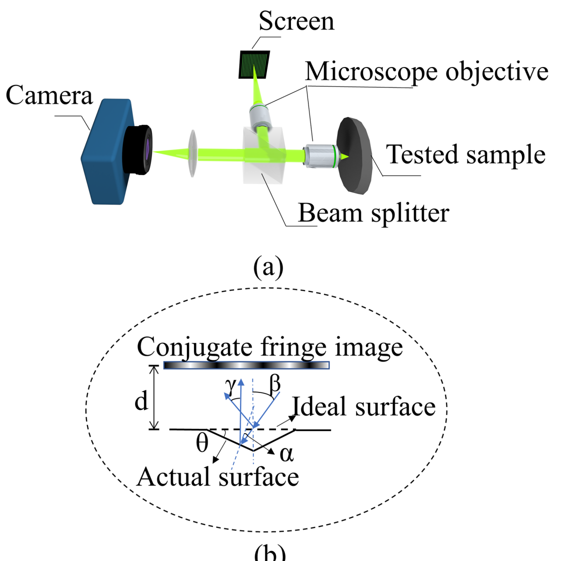


Fig. 1. Schematic of the PMDM: (a) System layout and (b) Measurement principle.

focusing and localization. But this is difficult to be realized for the in-situ and in-line measurement.

In this paper, the phase-measuring deflectometric microscopy (PMDM) is adopted for the fast measurement of micro scaled defects on specular surfaces. Phase Measuring Deflectometry (PMD) is a powerful measurement tool, which specifies the surface slopes based on the law of reflection/refraction and then reconstructs the surface form by integrating the gradients [15]. A microscopic objective lens can be employed to improve the lateral resolution. As the microscopic imaging has a limited DOF, a pinhole camera model is usually adopted in PMD to enlarge the DOF and release the requirement for precise focusing. The gradient-based measuring strategy indicates its potential for local defect inspection. The structural simplicity and flexibility make it suitable for in-situ measurement [16].

This paper is organized as follows. The methodology is presented in Section II, the simulation and experiment are presented in Section III, and finally, the paper is summarized in Section IV.

## II. Measurement Methodology

### A. Measurement Principle

Fig. 1(a) Shows a schematic diagram of the PMDM configuration. In this system, a screen generates a fringe pattern reflected by a beam splitter (BS). The conjugate fringe image produced by the combination of the two microscopic objectives and the BS is at a distance $d$ from the sample under test. A distorted fringe image is reflected by the sample, and then collected by the microscopic objective and finally imaged on a camera. Using the sinusoidal fringe illumination and the phase-shifting algorithm [17], [18] the phase distribution corresponding to the distorted fringes can be obtained. Subsequently, the slope data can be quantitatively obtained via the retrieved phases**.** As depicted in Fig. 1(b), $\theta$ is the slope angle of the measurement point, and $\alpha$ and $\beta$ are the actual and ideal incident angles respectively. $\gamma$ represents the difference between the ideal angle and the actual angle of reflection, which is resulting from the defect. It is easy to obtain that $\alpha + \theta = \beta$ and $\gamma + 2\alpha = 2\beta$, from which $\gamma = 2\theta$ can be deduced. Hence, the relation between the defect slope and phase deviation can be represented as

$$\Delta\varphi = 2\pi/p \cdot d \cdot \theta \tag{1}$$

where $d$ represents the distance between the sample under test and the conjugate fringe image, and $p$ denotes the period of the fringe. Given that the parallelism between different planes in the system has been carefully tuned, $d$ is a constant over the whole measurement field. Then $d$ can be calibrated using a laser displacement sensor. First, the sample is placed at a position $z_1$ where the virtual fringe pattern reflected by the sample is in-focus. Then, the sample is moved across the focal plane and stops at another position $z_2$. The scaling factor $d$ is two times the distance between $z_1$ and $z_2$. Thus, the calibration result of $d$ will not affect the morphologies, but the heights/depths of the defects will change proportionally.

The slope range $\Delta s$, lateral resolution $\delta x$ and vertical resolution $\Delta z$ are three important parameters governing the measurement system. The slope range $\Delta s$ is around 0.52 rad associated with the numerical aperture NA $= 0.25$ of the objective. The lateral resolution $\delta x$ is related to the angular measuring uncertainty $\delta\alpha$ as [18]:

$$\delta x \cdot \delta\alpha = \frac{\lambda}{Q} \tag{2}$$

where $\lambda$ is the wavelength of the light and $Q$ is a quality factor depending solely on the system signal-to-noise ratio (SNR) of the camera used. Consequently, the vertical resolution can be given by:

$$\Delta z = \frac{\delta x \cdot U_{pixel} \cdot P_{pixel}}{2d} \tag{3}$$

where $P_{pixel}$ is the pixel size of the screen after being reduced by the combination of microscopic objectives, and $U_{pixel}$ is the phase uncertainty introduced by phase retrieval, which is a function associated with the system SNR [19]. The lateral resolution is determined by the diffractive limit and defocusing associated with the microscopic objective and the discrete quantization effect associated with the camera pixel and the screen pixel. In accordance with the imaging relationship, one screen pixel corresponds to the width of nearly 2.05 camera pixels and 2.25 $\mu$m on the sample. Thus, the lateral resolution is 2.25 $\mu$m and it can be improved by adjusting the configuration. Then, the vertical resolution is ~0.789 nm corresponding to the phase uncertainty 1/50 pixel [19], [20].

In addition to the pinhole camera, the sinusoidal fringe also releases the requirement for precise focusing because it remains approximately sinusoidal when the image is defocused [21]. The DOF is determined in accordance with the normalized modulation coefficient $J(x, y)$, which directly measures the reliability of the retrieved phases[22]. According to (1), correct slopes could be worked out only with the phases retrieved reliably.

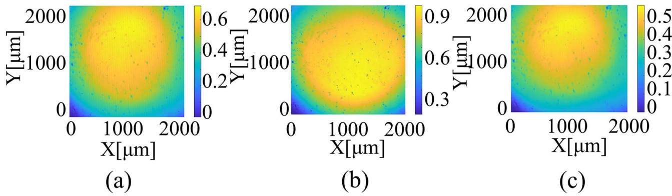


Fig. 2. Variation of $J(x, y)$ with $z$. (a) $z$ = -45 $\mu$m. (b) $z$ = -33.877 $\mu$m. (c) $z = 45$ $\mu$m.

The modulation $M(x, y)$ is defined as

$$M(x,y) = \sqrt{\left[\sum_{n=1}^{N} I_n(x,y)\sin(2\pi n/N)\right]^2 + \left[\sum_{n=1}^{N} I_n(x,y)\cos(2\pi n/N)\right]^2} \tag{4}$$

where $N$ represents the number of the phase-shifting steps, and $I_n$ denote the light intensity of the $n$-frame. $J(x, y)$ can be defined as

$$J(x,y) = \frac{M(x,y) - M_{\min}(x,y)}{M_{\max}(x,y) - M_{\min}(x,y)} \tag{5}$$

Therefore, an experiment could be carried out for locating the DOF. $d$ is 67.754 $\mu$m in practice. The sample is regarded within the DOF if more than 80% pixels have their $J(x, y)$ greater than the given threshold of 0.3. The exact focus plane is set as the origin and the positive direction is along the optical axis away from the system. For focus depths $z = -45$ $\mu$m, -33.877 $\mu$m and 45 $\mu$m, the modulation coefficients are as shown in Fig. 2, corresponding to 90.73%, 99.08% and 81.50%. pixels greater than the threshold, respectively. Hence, the DOF is $\sim$90 $\mu$m, which is twenty times that of conventional microscopic imaging under the same objective lens, and it can be enlarged by reducing the aperture.

### B. Topography Reconstruction

Numerical integration is then implemented to reconstruct surface topographies from the slopes calculated from (1). The integration methods used in PMD can be divided into two categories, namely the global methods [23], [24], [25], [26] and the local methods [27], [28]. Global methods conduct reconstruction by global optimization, in which case certain local features can be eliminated due to the underlying smoothing effect. As a contrary, local methods, such as the path integration techniques can maintain local features, but they are also sensitive to noise, and the reconstruction accuracy is affected by the integrating path. Therefore, a robust integration method is proposed. Before reconstruction, the gradient field is sparsely represented first to refine the non-integrable gradients; And then, the curl is taken as a quality factor to guide the integrating path.

For example, given four pixels (x, y), (x+1, y), (x+1, y+1), and (x, y+1), the heights of the four pixels can be integrated using the gradients in a clockwise loop, by taking the pixel $(x, y)$ as the start and the end. In this process, the resulting height of the pixel $(x, y)$ is assumed to be $z'(x, y)$. There would be a step at this pixel, if the sum of gradients along the integration loop is not zero, which is caused by the poor gradients provided. This sort of gradient field is non-integrable, which can be quantitively assessed using the curl information. This implies that, a gradient map is integrable if it has zero curl in the whole field [29], because most surfaces under test are continuous. But in practice, such a condition may not be satisfied due to inaccurate system calibration, erroneous slope calculation or the noise in measurement [30].

Thus, a non-integrable gradient field should be converted into an integrable one. In another word, it is converted into a global zero-curl field. Obviously, the measured gradient field $G$ can be considered a combination of an integrable gradient field $G_0$ and a rotational gradient field $Q$ associated with error and noise as $G = G_0 + Q$.

In a discrete domain, the curl is defined as:

$$C(x,y) = p(x,y+1) - p(x,y) + q(x,y) - q(x+1,y) \tag{6}$$

where $C(x, y)$ is a factor defined to evaluate the curl value associated with the pixel $(x, y)$ in the clockwise direction. $p$ and $q$ denote the gradients, which are defined as $p(x, y) = z(x+1, y) - z(x, y)$ and $q(x, y) = z(x, y+1) - z(x, y)$, respectively. Thus, imposing a curl operator $D$ on the gradient field $G$, the curl map can be described as,

$$C = DG = D(G_0 + Q) = DG_0 + DQ \tag{7}$$

where, (8) shown at the bottom of the next page.

And $D$ is a natural redundant dictionary. According to the condition $DG_0 = 0$, the equation becomes $DQ = C$. The gradient field $Q$ should be sparsely represented as a linear combination of $\|l\|_p^p$ constrained with $0 \le p \le 1$ and a sparse redundant dictionary $D$ [29]. Mathematically, the $\|l\|_0$ constraint is the intuitive sparsity indicator because it directly counts the number of nonzero entries in $Q$. But $\|l\|_1$ is usually applied here due to the NP-hard problem resulting from the $\|l\|_0$ constraint. The redundant dictionary $D$ satisfies the RIP condition [31], and thus $\|l\|_0$ can be relaxed by using $\|l\|_1$ as the sparsity constraint. Then, a sparse representation for gradient refinement is given as follows,

$$\hat{Q} = \arg\min \|Q\|_1, \|DQ - DG\|_2^2 \le \delta \tag{9}$$

where $\delta$ is a small threshold defined to terminate the iteration in optimization. Once $Q$ is obtained from the sparsest solution, a global curl-free gradient field $G_0$ can be solved. The selection of the integration path is critical to the reconstruction results. Several path-selecting strategies have been proposed for local path integration. Zhang [28] developed a cross-path integration method, which starts from the middle of the field, and then performs integration in the four quadrants. Wu [32] took two paths along the x and y directions and reduced errors by averaging. However, these traditional path integration methods have low accuracy due to a fixed integration path. The noise and error would propagate along the path.

Unfortunately, the curl of the retrieved gradient field $G_0$ cannot be exactly zero because of the sparse approximation in (8). Thus, by imposing the curl operator $D$ on the retrieved gradient field $G_0$, the newly obtained curl map $A$ can reflect the

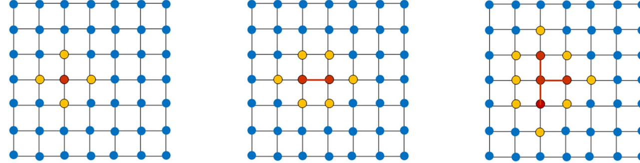

Fig. 3. The Minimum spanning tree integration method.

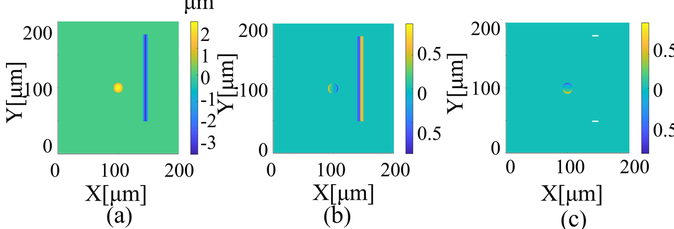


Fig. 4. The generated surface for simulation. (a) Specular surface with defects. (b) Gradient in *x* direction; (c) Gradient in *y* direction.

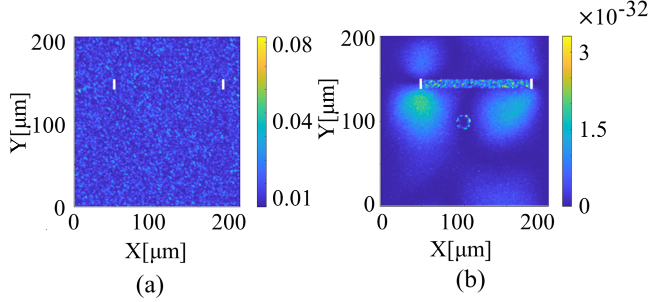


Fig. 5. The curls of noisy gradient fields. (a) Without sparse representation. (b) With sparse representation.

reliability of the resulting gradient field $G_0$. Consequently, it can be taken as a cost function to guide the integrating path.

A minimum spanning tree method is developed for designing an appropriate integration path. In this method, not all the gradients would be utilized for integration. A connected weighted graph $B = (V, E)$ is defined here, as depicted in Fig. 3. $V$ represents the nodes and $E$ denotes the edges, corresponding to pixels and gradients, respectively. $T = (U, TE)$ is the minimum spanning tree, where $U$ is the subset of $V$, and $TE$ is the set of edges in the tree. There would be $k$ nodes connected with $k$-1 edges in the tree. For an edge $(u, v)$ connecting two nodes $u$ and $v$, the weight is defined as the curl of the end node $v$. All the nodes are labelled blue in advance, indicating that they have not been calculated. While the calculated nodes are labelled red and the search scope, which is composed of the adjacent nodes of the red nodes, is colored yellow. The procedure to generate a minimum spanning tree is as follows,

*Step 1:* A node $u_0$ with lowest curl is taken as the starting point. Hence, the initial set of nodes is $\mathrm{U} = \{u_0\}(u_0 \in \mathrm{V})$, and the initial set of edges is $\mathrm{TE} = \{\}$. The nodes allocated in U and the edges allocated in TE are the calculated nodes and edges, respectively;

*Step 2:* Search for an edge $(u, v)$, where $v$ has the lowest-curl and it is labelled yellow. The height of node $v$ can be calculated using the gradient of edge $(u, v)$. Then the node and the edge would be added to the sets $U$ and $TE$, respectively.

*Step 3:* Repeat step 2 until $U = V$. That is to say, all the nodes are calculated.

The minimum spanning tree $T = (U, TE)$ can be achieved via the procedure. Thus, the topography of the sample is obtained in turn.

## III. Simulation and Experimental Demonstration

### A. Numerical Simulation

The feasibility of the sparse representation is verified first by a simulation. A surface with a V-shaped groove of a depth of 3 $\mu$m and a width of 10 $\mu$m and a small ellipsoidal feature with three half-axis lengths $a = 8$ $\mu$m, $b = 8$ $\mu$m and $c = 2$ $\mu$m is generated, as depicted in Fig. 4(a). The corresponding gradient maps in the $x$ and $y$ directions are shown in Fig. 4(b) and (c).

Gaussian noise is added on the gradient fields, with an average of zero and a standard deviation of 3% of the maximum gradient. The curl of the noisy gradient fields is depicted in Fig. 5(a), while the curl map $A$ associated with the method in Section II-B is depicted in Fig. 5(b). The curl of the whole field is almost zero and it well indicates the quality of the local gradients, especially in the edge of the defects. Consequently, the minimum spanning

$$D = \begin{bmatrix} -1 & 0 & \dots & 1 & 0 & \dots & 1 & -1 & 0 & \dots & \dots & 0 \\ 0 & -1 & 0 & \dots & 1 & 0 & \dots & 1 & -1 & 0 & \dots & 0 \\ \vdots & \vdots & \vdots & \vdots & \vdots & \vdots & \vdots & \vdots & \vdots & \vdots & \vdots & \vdots \\ 0 & \dots & \dots & \dots & -1 & 0 & \dots & 1 & 0 & \dots & 1 & 1 \end{bmatrix}_{(M-1)(N-1)\times 2MN},$$

$$G = \begin{bmatrix} p(1,1) \\ p(1,2) \\ \vdots \\ p(m,n) \\ q(1,1) \\ q(1,2) \\ \vdots \\ q(m,n) \end{bmatrix}_{2MN\times 1}, C = \begin{bmatrix} C(1,1) \\ C(1,2) \\ \vdots \\ C(m-1,n-1) \end{bmatrix}_{(M-1)(N-1)\times 1}. \tag{8}$$

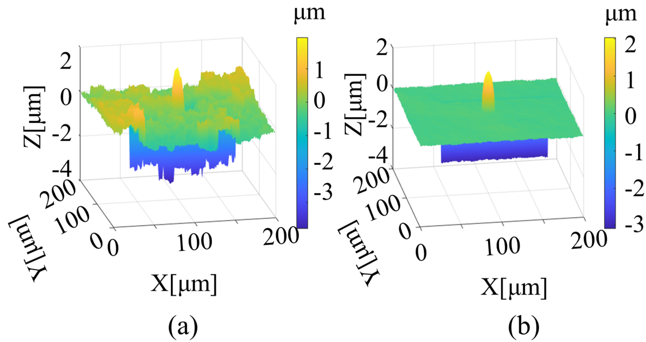

Fig. 6. The reconstruction results using different methods. (a) Without sparse representation. (b) With sparse representation.

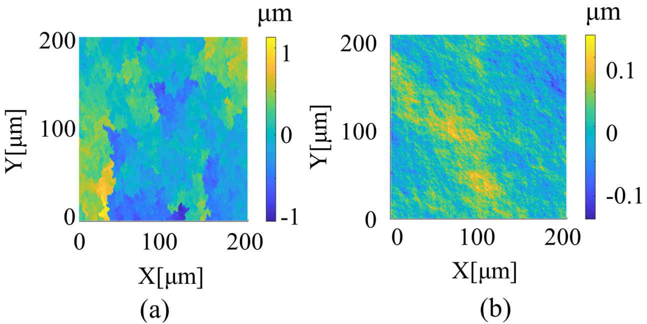

Fig. 7. The reconstruction errors using different methods. (a) Without sparse representation. (b) With sparse representation.

tree can be established under the guide by the curl, making sure that the resulting integration path crosses the defect boundaries the fewest times. The resulting integration errors would be the minimum in this case. Additionally, the sparse representation reduces the effect of noise in different measurements. This effectively guarantees the reproducibility of the reconstruction.

Then the minimum spanning trees without and with sparse representation are applied to evaluate the reconstruction accuracy, by taking the residual curls in Fig. 5 as the cost function. The reconstruction results are depicted in Fig. 6 and the errors are shown in Fig. 7. The reconstructed results show that the topography of the local defects can be well obtained, especially for the bottom line of the V-shaped groove. And the errors are only dozens of nanometers.

### B. Experimental Verification

To experimentally verify the proposed method, a deflectometric microscope system is built as shown in Fig. 8. The camera is Allied Vision Manta G-419 with a resolution of 2048 × 2048 pixels, and a cell size of 5.5 × 5.5 $\mu$m. A high-luminance Micro-OLED screen (luminance: 3000 cd/m$^2$) is adopted in the system to improve the SNR. The resolution of the screen is 1920 × 1080 pixels with a pixel size of 5.616 × 5.616 $\mu$m. A 10x objective is applied on the sample side and a 4x objective is installed on the screen side. The combination of objectives not only minifies the pixel size in the (3) to gain a better vertical resolution but also ensures a measurement region of 2.2 mm. A germanium plate is used as a sample in the experiment below. And there are three

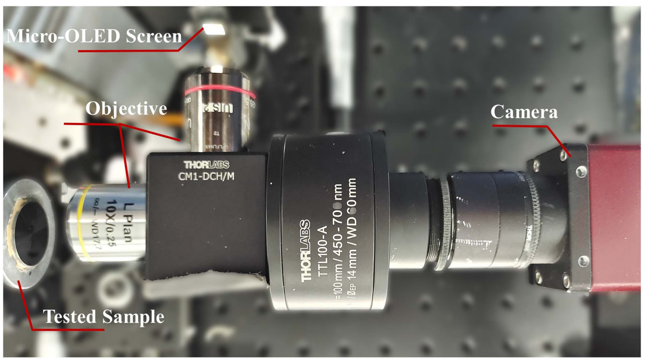


Fig. 8. Setup of the deflectometric microscope system.

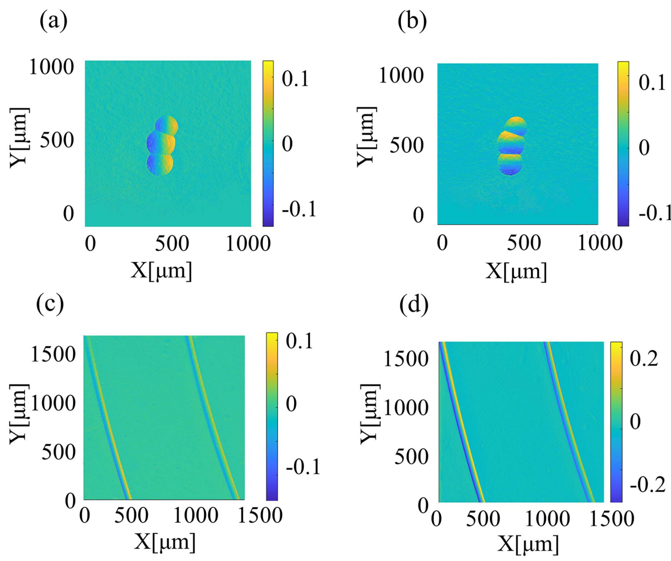

Fig. 9. The gradient data. (a) Three pits in $x$ direction. (b) Three pits in $y$ direction. (c) Two V-shaped grooves in $x$ direction. (d) Two V-shaped grooves in $y$ direction.

pits and two V-shaped grooves on the germanium surface. The distance $d$ in (1) is calibrated with a laser displacement sensor HCL-L15 with a resolution of 0.25 $\mu$m.

$\Delta\varphi$ in (1) is acquired by subtracting the ideal phase, which is achieved by placing a standard mirror in focus, from the actual phase retrieved from the captured images. Before that, a three-step phase-shifting algorithm and a modified three-frequency algorithm are applied to retrieve the absolute phase value. Five frames need to be taken, i.e., three for the highest frequencies, from which the light intensity, the modulation intensity, and the wrapped phase can be obtained, and one for each of the remaining frequencies. Thus, the other two wrapped phases can be solved with the light intensity and the modulation intensity, and the absolute phase can be retrieved. Therefore, the slope angle $\theta$ can be obtained by solving (1). After that, the integrable gradient data can be achieved by sparse representation, as depicted in Fig. 9.

Using the proposed reconstruction method, the topography of the tested sample could be obtained. In order to verify the accuracy of the proposed method, a Taylor Hobson CCI MP

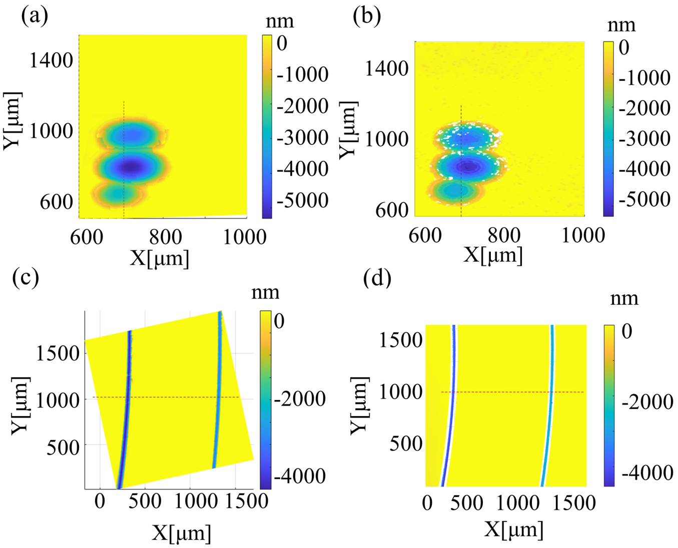


Fig. 10. Comparison of the measured topographies. (a) The proposed method for three pits. (b) CCI for three pits. (c) the proposed method for two grooves. (d) CCI for two V-shaped grooves.

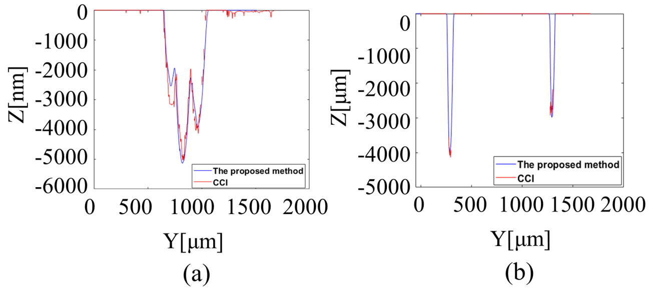


Fig. 11. Comparison of profiles. (a) Three pits. (b) Two V-shaped grooves.

is used to measure the topography as a comparison, as shown in Fig. 10. The null points in Fig. 10(b) could be caused by weak reflection on the rough surface, which results in a poor fringe and a low SNR. While in Fig. 10(d), null occurs mostly due to the limited measurable range of CCI, which in turn reveals the high measurable range of the proposed method. Comparison of those profiles is depicted using red dashed lines in Fig. 11.

The profile comparison demonstrates that the proposed method can obtain the topography of micro-nano defects with a small deviation compared to the result of the CCI. This deviation may be mainly caused by the convolution problem concerning defocusing and aberrations in the image system [33], [34]. But it is acceptable considering its advantage of high dynamic range and high efficiency.

## IV. Summary

This paper presents a fast topography measuring strategy based on the deflectometric microscopy. Because the pinhole model and the sinusoidal fringe release the requirement for precise focusing, a DOF of 90 $\mu$m could be achieved in this measurement system, which is superior to the conventional microscopy and makes it promising for fast in-situ measurement. Furthermore, a sparse representation retrieves the integrable gradient fields, and then, the minimum spanning tree is implemented to reconstruct the topography quantitatively. Contamination and discontinuity degrade the phase modulation and cause measurement errors, and this issue needs further investigation. This method can improve the accuracy, efficiency, and flexibility of defect measurements, and it is of great significance in the field of quality control for ultra-precision manufacturing.

## References


[1] A. Mital, M. Govindaraju, and B. Subramani, “A comparison between manual and hybrid methods in parts inspection: IMS,” *Integr. Manuf. Syst.*, vol. 9, pp. 344–349, 1998.

[2] H.-Y. Zhang, Z.-H. Wang, and H.-Y. Fu, “Automatic scratch detector for optical surface,” *Opt. Exp.*, vol. 27, no. 15, pp. 20910–20927, 2019.

[3] Y. Hara, N. Akiyama, and K. Karasaki, “Automatic inspection system for printed circuit boards,” *IEEE Trans. Pattern Anal. Mach. Intell.*, vol. PAMI-5, no. 6, pp. 623–630, Nov. 1983.

[4] L. Ri-Xian, Y. Ming-Hai, and W. Xian-Bao, “Defects detection based on deep learning and transfer learning,” *Metallurgical Mining Ind.*, vol. 2015, pp. 312–3231, Jul. 2015.

[5] R. Ren, T. Hung, and K. C. Tan, “A generic deep-learning-based approach for automated surface inspection,” *IEEE Trans. Cybern.*, vol. 48, no. 3, pp. 929–940, Mar. 2018.

[6] F. Wu et al., “Classification between digs and dust particles on optical surfaces with acquisition and analysis of polarization characteristics,” *Appl. Opt.*, vol. 58, no. 4, pp. 1073–1083, Feb. 2019.

[7] V. M. Schneider, M. Mlejnek, and K. T. Gahagan, “Fast detection of single-sided diffracted defects in display glass,” *Measurement*, vol. 42, no. 4, pp. 638–644, May 2009.

[8] D. Liu et al., “Dark-field microscopic image stitching method for surface defects evaluation of large fine optics,” *Opt. Exp.*, vol. 21, pp. 5974–5987, Mar. 2013.

[9] K. Rebner et al., “Dark-field scattering microscopy for spectral characterization of polystyrene aggregates,” *Opt. Exp.*, vol. 18, pp. 3116–3127, Feb. 2010.

[10] Y. Li, Q. L. Wang, Y. F. Li, X. De, and M. Tan, “On-line visual measurement and inspection of weld bead using structured light,” in *Proc. IEEE Instrum. Meas. Technol. Conf.*, 2008, pp. 2038–2043.

[11] Y. Huang, H. Yue, Y. Fang, W. Wang, and Y. Liu, “Structured-light modulation analysis technique for contamination and defect detection of specular surfaces and transparent objects,” *Opt. Exp.*, vol. 27, pp. 37721–37735, 2019.

[12] T. Guo et al., “Development of a hybrid atomic force microscopic measurement system combined with white light scanning interferometry,” *Sensors*, vol. 12, no. 1, pp. 175–188, 2011.

[13] G. Sandra, H. Kenneth, B. Justin, and G. Brian, “Measurements of surface defects on optical components,” *Meas. Sci. Technol.*, vol. 9, Apr. 1998, Art. no. 607.

[14] W. Yang et al., “A novel white light interference based AFM head,” *J Lightw. Technol.*, vol. 35, pp. 3604–3610, Aug. 2017.

[15] J. Ye, Z. Niu, X. Zhang, W. Wang, and M. Xu, “In-situ deflectometic measurement of transparent optics in precision robotic polishing,” *Precis. Eng.*, vol. 64, pp. 63–69, Jul. 2020.

[16] T. Chen, Y. Chen, X. Zhang, W. Wang, and M. Xu, “Workpiece positioning and error decoupling in the single-point diamond turning of freeform mirrors based on the monoscopic deflectometry,” *Precis. Eng.*, vol. 77, pp. 16–23, Sep. 2022.

[17] C. K. Markus, K. Jurgen, and H. Gerd, “Phase measuring deflectometry: A new approach to measure specular free-form surfaces,” *Proc. SPIE*, vol. 5457, 2004, pp. 366–376.

[18] G. Häusler, C. Richter, K.-H. Leitz, and M. C. Knauer, “Microdeflectometry—A novel tool to acquire three-dimensional microtopography with nanometer height resolution,” *Opt. Lett.*, vol. 33, pp. 396–398, Feb. 2008.

[19] P. Su, R. E. Parks, L. Wang, R. P. Angel, and J. H. Burge, “Software configurable optical test system: A computerized reverse Hartmann test,” *Appl. Opt.*, vol. 49, pp. 4404–4412, 2010.

[20] H. Gu et al., “High-accuracy deflectometric microscope system with a large slope range,” *Opt. Lett.*, vol. 46, pp. 2011–2014, 2021.

[21] C. Zuo, S. Feng, L. Huang, T. Tao, W. Yin, and Q. Chen, “Phase shifting algorithms for fringe projection profilometry: A review,” *Opt. Lasers Eng.*, vol. 109, pp. 23–59, 2018.

[22] X.-Y. Su, G. Von Bally, and D. Vukicevic, “Phase-stepping grating profilometry: Utilization of intensity modulation analysis in complex objects evaluation,” *Opt. Commun.*, vol. 98, pp. 141–50, 1993.

[23] J. Campos, L. P. Yaroslavsky, A. Moreno, and M. J. Yzuel, “Integration in the Fourier domain for restoration of a function from its slope: Comparison of four methods,” *Opt. Lett.*, vol. 27, pp. 1986–1988, 2002.

[24] L. Huang and A. Asundi, “Improvement of least-squares integration method with iterative compensations in fringe reflectometry,” *Appl. Opt.*, vol. 51, pp. 7459–7465, 2012.

[25] G. Li, Y. Li, K. Liu, X. Ma, and H. Wang, “Improving wavefront reconstruction accuracy by using integration equations with higher-order truncation errors in the southwell geometry,” *J. Opt. Soc. Amer. A*, vol. 30, pp. 1448–1459, 2013.

[26] J. Ye et al., “Modal wavefront estimation from its slopes by numerical orthogonal transformation method over general shaped aperture,” *Opt. Exp.*, vol. 23, pp. 26208–26220, 2015.

[27] X. Jing, H. Cheng, and Y. Wen, “Path integration guided with a quality map for shape reconstruction in the fringe reflection technique,” *Meas. Sci. Technol.*, vol. 29, 2018, Art. no. 045011.

[28] H. Zhang, S. Han, S. Liu, S. Li, L. Ji, and X. Zhang, “3D shape reconstruction of large specular surface,” *Appl. Opt.*, vol. 51, no. 31, pp. 7616–7625, 2012.

[29] Y.-L. Xiao, S. Li, Q. Zhang, J. Zhong, X. Su, and Z. You, “Optical fringe-reflection deflectometry with sparse representation,” *Opt. Lasers Eng.*, vol. 104, pp. 62–70, 2018.

[30] X. Jing, H. Cheng, Y. Wen, K. Gao, H. Wang, and H. Yang, “Shape reconstruction based on zero-curl gradient field estimation in a fringe reflection technique,” *Appl. Opt.*, vol. 57, no. 15, pp. 4135–4144, 2018.

[31] E. J. Candes, J. Romberg, and T. Tao, “Robust uncertainty principles: Exact signal reconstruction from highly incomplete frequency information,” *IEEE Trans. Inf. Theory*, vol. 52, no. 2, pp. 489–509, Feb. 2006.

[32] Z. Wu and L. Li, “A line-integration based method for depth recovery from surface normals,” *Comput. Vis., Graph., Image Process.*, vol. 43, no. 1, pp. 53–66, 1988.

[33] Z. Niu, J. Wang, Y. Tian, Z. Wu, C. Wei, and J. Shao, “Wavefront-coded phase measuring deflectometry for the all-focused measurement,” *Opt. Lett.*, vol. 47, no. 18, pp. 4770–4773, 2022.

[34] Y. Chen, X. Zhang, T. Chen, R. Zhu, L. Ye, and W. Lang, “Transition imaging phase measuring deflectometry for high-precision measurement of optical surfaces,” *Meas.*, vol. 199, 2022, Art. no. 111589.